Giant nonlinear anomalous Hall effect induced by spin-dependent band structure evolution

Xiangyu Cao,[1,*] Jie-Xiang Yu,[2,3,*] Pengliang Leng,[1,*] Changjiang Yi,[4,5,*] Xiaoyang Chen,[1,6] Yunkun Yang,[1] Shanshan Liu,[1] Lingyao Kong,[8] Zihan Li,[1] Xiang Dong,[1] Youguo Shi,[4] Manuel Bibes,[7] Rui Peng,[6,11] Jiadong Zang,[2,†] and Faxian Xiu[1,9,10,11,‡]

[1]*State Key Laboratory of Surface Physics and Department of Physics, Fudan University, Shanghai 200433, China*
[2]*Department of Physics and Astronomy, University of New Hampshire, Durham, New Hampshire 03824, USA*
[3]*Department of Physics, University of Florida, Gainesville, Florida 32611, USA*
[4]*Beijing National Laboratory for Condensed Matter Physics, Institute of Physics, Chinese Academy of Sciences, Beijing 100190, China*
[5]*University of Chinese Academy of Sciences, Beijing 100049, China*
[6]*Laboratory of Advanced Materials, Fudan University, Shanghai 200433, China*
[7]*Unité Mixte de Physique, CNRS, Thales, Université Paris-Saclay, 91767 Palaiseau, France*
[8]*School of Physics and Materials Science, Anhui University, Hefei, 230601, China*
[9]*Shanghai Qi Zhi Institute, 41st Floor, AI Tower, No. 701 Yunjin Road, Xuhui District, Shanghai, 200232, China and Institute for Nanoelectronic Devices and Quantum Computing, Fudan University, Shanghai 200433, China*
[10]*Zhangjiang Fudan International Innovation Center, Fudan University, Shanghai 201210, China*
[11]*Shanghai Research Center for Quantum Sciences, Shanghai 201315, China*

(Received 8 February 2021; accepted 7 March 2022; published 6 May 2022)

The anomalous Hall effect (AHE) is a key transport signature revealing the topological properties of magnetic compounds. In quantum materials, the classical linear dependence of the AHE on magnetization often breaks down, which is typically ascribed to the presence of topological magnetic or electronic textures. However, the complex electronic structure of these compounds may offer alternative, unexplored mechanisms. Here, we show that a giant nonlinear AHE can originate from a series of magnetic-field-induced Lifshitz transitions in the spin-dependent band structure. In our experiments on $EuCd_2As_2$ the AHE contributes to 97% of the total Hall response, corresponding to a record anomalous Hall angle of 21%. Our scaling analysis and first-principles calculations demonstrate that the electronic structure is extremely sensitive to spin canting, with the magnetic field causing band crossing and band inversion and introducing a band gap when oriented along specific directions. Our results not only provide an ideal platform for Berry curvature engineering but reveal a general effect that may be applied to other material systems.

DOI: 10.1103/PhysRevResearch.4.023100

I. INTRODUCTION

The anomalous Hall effect (AHE) is a vital transport signature connecting electron properties and magnetic orders in magnetic materials. While it is assumed to show a linear relation with magnetization (M) in most cases [1], the nonlinearity of AHE has only been observed under strict conditions [1,2]. The most celebrated nonlinear AHE is the topological Hall effect (THE), which can be viewed as a special kind of AHE induced by real-space spin chirality [2–8]. In noncoplanar spin textures such as magnetic skyrmions, the nonzero scalar chirality $\chi_{ijk} = S_i \cdot (S_j \times S_k)$ generates a finite real-space Berry phase, acting as an effective magnetic field on conduction electrons [3], and leads to the topological Hall resistivity. Due to its unique pronounced peak feature, it has been widely used as a direct fingerprint of chiral spin structures [9,10]. On the other hand, the concept of nonlinear AHE has also been extended to the intrinsic part of AHE in topological semimetals. It is induced by the amplified Berry curvature around Weyl nodes, and the AHE can then deviate from linearity as reported in a limited number of systems [11–17]. These two mechanisms require special magnetic or electron structures and it is thus interesting to explore the existence of nonlinear AHE in a wider range of materials. It is, however, quite challenging since different mechanisms are often intertwined and a clear separation is hardly achievable [18–20]. Furthermore, spin structures could strongly affect band structures, hampering a deep understanding of the nonlinear AHE.

Here we report a giant nonlinear AHE showing pronounced peaks in $EuCd_2As_2$ with the largest resistivity $\rho_{xy}^{NA} = 383.5\ \mu\Omega\,\mathrm{cm}$, which makes up for 97% of the total Hall resistivity and fully dominates the Hall response. This giant nonlinear AHE resembles the THE in systems with chiral spin textures, raising a question of its physical origin. A

*These authors contributed equally to this work.
†Jiadong.Zang@unh.edu
‡Faxian@fudan.edu.cn

Published by the American Physical Society under the terms of the Creative Commons Attribution 4.0 International license. Further distribution of this work must maintain attribution to the author(s) and the published article's title, journal citation, and DOI.

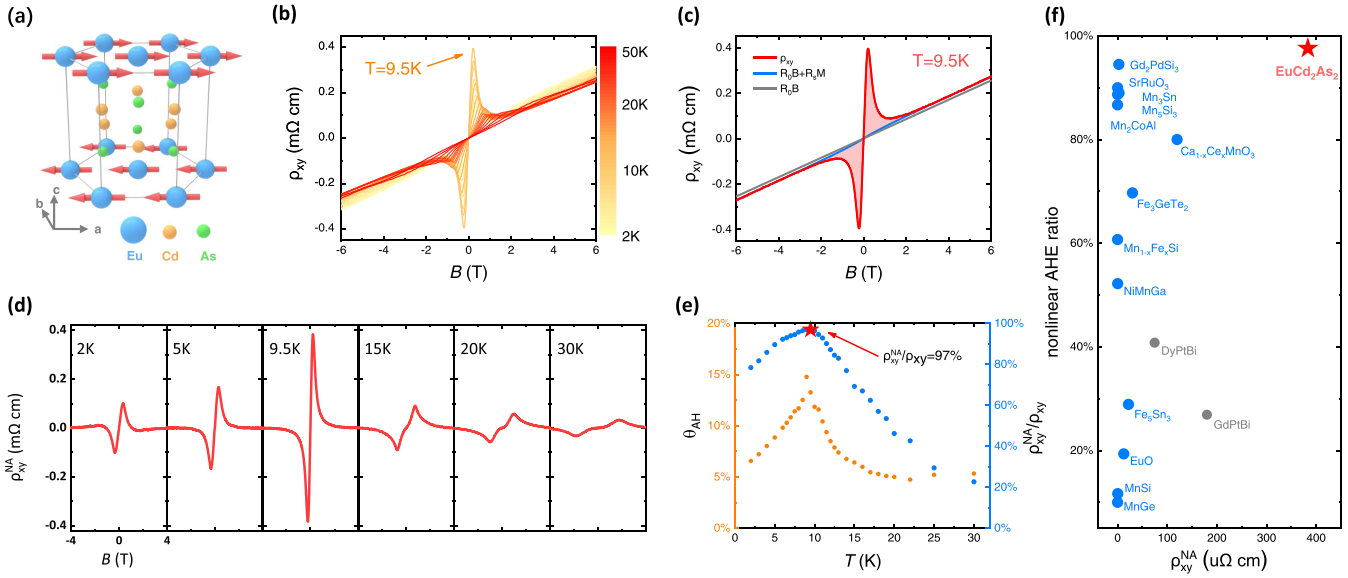

FIG. 1. Temperature-dependent nonlinear AHE in $EuCd_2As_2$. (a) Crystal structure of $EuCd_2As_2$. (b) Magnetic-field dependence of the Hall resistivity ρ_{xy} at different temperatures. (c) Decomposition of the field-dependent Hall resistivity measured at $T = 9.5$ K. The red line is the original Hall resistivity. The blue line is the sum of the ordinary Hall effect and conventional AHE $R_0B + R_sM$. The red zone corresponds to AHE nonlinear to M. (d) Magnetic-field dependence of the nonlinear AHE resistivity ρ_{xy}^{NA} at various temperatures from 2 to 30 K. (e) Maximum anomalous Hall angle (yellow) and nonlinear AHE ratio (blue) at different temperatures. The nonlinear AHE contributes 97% of the total Hall signal at $T = 9.5$ K. (f) Nonlinear AHE ratio and ρ_{xy}^{NA} of THE systems (blue) and nonlinear intrinsic AHE systems (gray). All data here were measured with $B \parallel c$ and $I \parallel a$.

similar feature was reported in $EuCd_2As_2$ in recent studies [18,21–23] and attributed to the presence of Weyl nodes near the Fermi level [18]. Alternatively, in samples with a lower Fermi energy and thus unaffected by Weyl nodes, we find a more pronounced THE-like feature and show that it is caused by the spin-rotation-induced band structure evolution under an external magnetic field. The direction of the spins plays an important role in the evolution of the band structure, causing band inversions and gap opening at certain canting angles, which results in a significant enhancement of the Berry curvature responsible for the AHE. Moreover, the ρ_{xy}^{NA} and the anomalous Hall angle can be further enhanced by tilting the magnetic field 30° away from the [001] direction. Particularly at low temperature ($T = 2$ K), both values increase from 100 $\mu\Omega$ cm and 5% to 430 $\mu\Omega$ cm and 21%, respectively, indicating that the momentum-space Berry curvature changes not only with the intensity but also the direction of the external magnetic field. Our results suggest the same phenomena should be observed in a wide range of magnetic materials without any special magnetic or electron structures.

II. RESULTS

$EuCd_2As_2$ was theoretically predicted and experimentally demonstrated to be a magnetic Weyl semimetal [21–27]. As shown in Fig. 1(a), $EuCd_2As_2$ has a trigonal crystal structure with a space group $P\bar{3}m1$ (no. 164). The crystal has a layered structure consisting of alternating triangular Eu layers and Cd_2As_2 bilayers. Eu atoms contribute to the magnetism in this system, forming an in-plane A-type antiferromagnetic (AFM) structure below the Néel temperature $T_N = 9.5$ K [21,28]. We performed first-principles calculations and magnetization measurements (see Fig. S2 in the Supplemental Material [29]) to confirm the magnetic properties. According to the total energy analysis, the antiferromagnetic spin-ordering is 0.8 meV (9.3 K) lower in total energy than the ferromagnetic spin ordering. The spin-ordering with the in-plane Néel vector is 0.39 meV in total energy lower than the out-of-plane Néel vector. Besides, all of our measurements give no hysteresis behavior (Fig. S2 [29]). The in-plane antiferromagnetic spin ordering is thus the ground state, consistent with previous experimental observations [21].

As the central result of this work, the detailed temperature-dependent transport measurements with the external magnetic field applied along the [001] direction are shown in Figs. 1(b)–1(f). The Hall resistivity $\rho_{xy}(B)$ in Fig. 1(b) shows a prominent double-peak feature. When temperature increases from 2 to 50 K, the peaks are first enhanced, reaching a maximum value at $T = 9.5$ K, then suppressed at higher temperatures and almost invisible at $T > 50$ K. Compared to the $M(B)$ curve in the Supplemental Material [29], the pronounced two peaks near zero magnetic field in the original $\rho_{xy}(B)$ curves clearly deviate from linearity in magnetization.

The total Hall resistivity is expressed as $\rho_{xy} = R_0B + R_sM + \rho_{xy}^{NA}$, where the ρ_{xy}^{NA} term represents the AHE nonlinear in M. ρ_{xy}^{NA} with two peaks as observed here is conventionally regarded as the footprint of a typical real-space THE, but it can contain intrinsic AHE from the momentum-space Berry phase as well. The original Hall signal at $T = 9.5$ K [Fig. 1(c)] shows a giant nonlinear AHE (red area), which can be obtained after subtracting the ordinary Hall effect (OHE) and the conventional AHE (blue line) from the original Hall resistivity (red line) by fitting the original Hall data from $B = 4$ to 6 T to the equation $R_0B + R_sM$. The maximum $\rho_{xy}^{NA} = 383.5$ $\mu\Omega$ cm appearing at $B^* = \pm 0.2$ T is

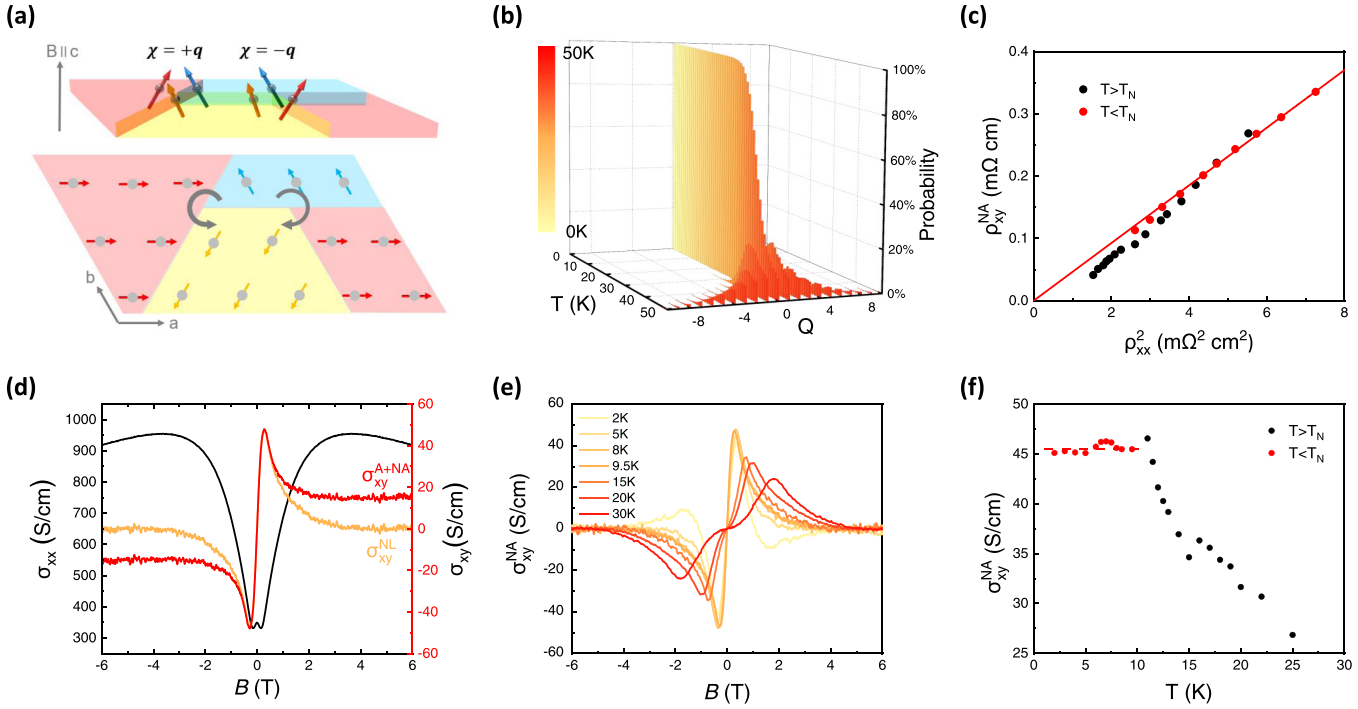

FIG. 2. Detailed analysis of nonlinear AHE in $EuCd_2As_2$. (a) Domain structure and the neutralization of overall scalar chirality in $EuCd_2As_2$. (b) Topological charges in $EuCd_2As_2$ at different temperatures. (c) Maximum ρ_{xy}^{NL} as a function of ρ_{xx}^2. The red line is the linear fitting for $T<T_N$. (d) Magnetic-field-dependent longitudinal conductivity (black line), nonlinear anomalous Hall conductivity (yellow line), and nonordinary Hall conductivity (red line) at $T = 9.5$ K. (e) Magnetic-field-dependent nonlinear anomalous Hall conductivity at different temperatures. (f) Nonlinear anomalous Hall conductivity at different temperatures.

five orders of magnitude larger than the saturation anomalous Hall resistivity. Furthermore, the nonlinear AHE ratio defined as $\frac{\rho_{xy}^{NA}}{|\rho_{xy}^{O}|+|\rho_{xy}^{A}|+|\rho_{xy}^{NA}|}$ (equal to ρ_{xy}^{NA}/ρ_{xy} for our system) reaches 97%, indicating that this feature completely dominates the Hall response at the peak position. The ρ_{xy}^{NA} at different temperatures [Fig. 1(d)] was extracted by the same procedure. Figure 1(e) presents the nonlinear AHE ratio and the calculated anomalous Hall angle $\theta_{AH} = 1-\sigma_{xy}^{O}/\sigma_{xx}$ at different temperatures. It always contributes more than 75% of the total Hall signal below 15 K and the maximum Hall angle reaches 16%, showing a prevailing response. We also use different ways to decompose the Hall conductivity and calculate the anomalous Hall angle (Fig. S4 [29]), which shows a similar result. In Fig. 1(f), we compare our results with previous reports of nonlinear AHE systems, including THE systems [4–8,30–37] and nonlinear intrinsic AHE [14,15]. The data of the related systems are estimated from Refs. [4–8,14,15,26–28,31–34]. The diagram highlights the salient nonlinear AHE feature in $EuCd_2As_2$ with a giant contribution ratio and ρ_{xy}^{NA}.

We now discuss the origin of the nonlinear AHE in $EuCd_2As_2$ and first consider whether it can be due to chiral spin textures. Eu atoms have a magnetic moment close to $7\mu_B$ [21], showing a large exchange interaction with conduction electrons, so that the adiabatic limit is respected. If a net chirality were to exist, it should contribute to the THE-like nonlinear AHE. However, $EuCd_2As_2$ has a point group $\bar{3}m1$ so that the spatial inversion is a lattice symmetry. Furthermore, the midpoint between any pair of neighboring Eu atoms is always an inversion center, so the Dzyaloshinskii-Moriya interaction is absent everywhere. The only possible spin canting takes place at domain walls. Previous x-ray observations indicated the possible presence of magnetocrystalline anisotropy in the plane, leading to three types of domains pointing 120° away from one another [21]. Once an external magnetic field is applied, spins tilt up, and spin canting emerges at the triple point where three domains meet. However, since the three-domain variants have equal populations, there are the same number of triple points with in-plane spins rotating clockwise and counterclockwise, so that the overall scalar chirality is zero. In fact, moving along a domain wall from any triple point, one always arrives at another triple point where spin rotates oppositely [Fig. 2(a)]. Our Monte Carlo calculations support this argument. As shown in Fig. 2(b), at finite temperatures, populations of topological charges $\pm Q$ are the same. We thus conclude that there is no real-space Berry phase in this system, and the observed nonlinear AHE is not a real space THE.

This conclusion is further supported by the scaling analysis of transport data. For the real-space Berry phase driven THE, the resistivity is related to the emergent magnetic field generated by the scalar chirality B_{eff} by $\rho_{xy}^{T} = \frac{B_{\text{eff}}}{ne}$, with n the carrier density and e the electron charge. It thus does not scale with the longitudinal resistivity ρ_{xx}. On the other hand, the momentum-space Berry phase contributes to the intrinsic Hall conductivity $\sigma_{xy}^{I} = \frac{e^2}{\hbar}\sum_n \int \frac{dk}{(2\pi)^3} b_n(\boldsymbol{k})$, where $b_n(\boldsymbol{k})$ is the Berry curvature of band n and $\hbar$ is the reduced Planck constant. It contributes to the Hall resistivity through $\rho_{xy}^{I} = \sigma_{xy}^{I}/(\sigma_{xy}^2+\sigma_{xx}^2)$. In metallic systems [1], $\sigma_{xx} \gg \sigma_{xy}$, so the

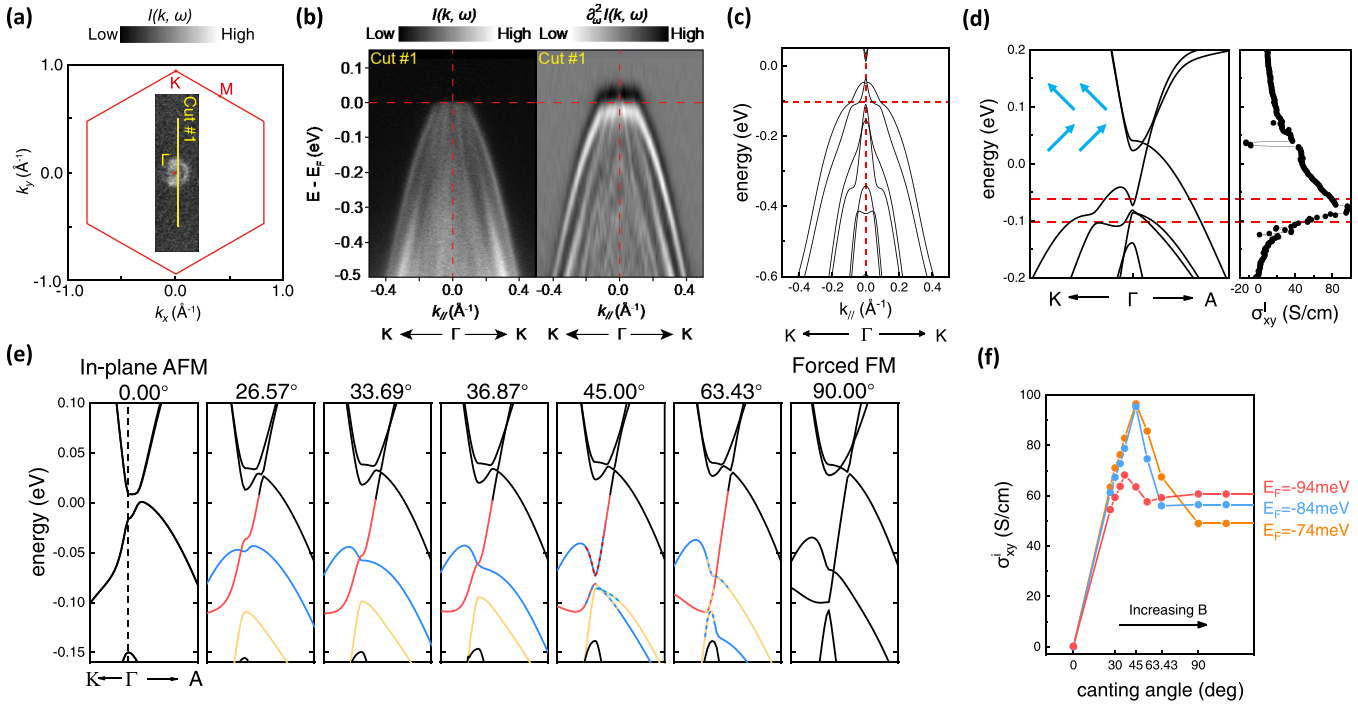

FIG. 3. ARPES measurements and the theoretical calculation results of $EuCd_2As_2$. (a) Photoemission intensity map at the Fermi energy (E_F) of $EuCd_2As_2$ integrated over an energy window of [E_F–50 meV, E_F + 50 meV]. The data were measured using 36.6 eV photons at the high symmetric Γ-*K*-*M* plane determined by photon-energy-dependent ARPES measurements. (b) Measured band structure (left) and the second derivative with respect to energy (right) along the Γ-*K* direction at $T = 7.9$ K. The momentum location of the cut is shown in panel (a). (c) Calculated band structure along the *K*-Γ-*K* direction with a canting angle of 26.57 °. The red line is the estimated real Fermi energy compared with the ARPES results. (d) Calculated band structure along the *K*-Γ-A direction and the corresponding energy-dependent intrinsic Hall conductivities σ^I_{xy} with a canting angle of 45°. Fermi energy lies between two red lines (–80 and −100 meV) estimated from the ARPES results. (e) Calculated band structures along the *K*-Γ-A direction with various canting angles. (f) Canting-dependent $|\sigma^I_{xy}|$ at various Fermi energies.

Hall resistivity ρ^I_{xy} is proportional to $\sigma^{-2}_{xx} \approx \rho^2_{xx}$ and σ^I_{xy} is constant. These two scaling relations are widely viewed as important signatures of an intrinsic AHE.

The temperature-dependent ρ^{NA}_{xy} (from Fig. 1) as a function of ρ^2_{xx} is shown in Fig. 2(c). The data measured at $T < T_N$ are very well fitted by a linear scaling, giving strong evidence of the momentum-space origin of the nonlinear AHE in $EuCd_2As_2$. Then we decompose the measured resistivity σ_{xy} in different components in Figs. 2(d) and 2(e). After substrating the scattering-related component σ_{xx}, the magnetic field dependence of σ^{NA}_{xy} still shows a prominent peak, indicating that the nonlinear AHE in this system is intrinsic. The peak values in $\sigma^{NA}_{xy}(B)$ are almost independent of temperature and σ_{xx} for $T < T_N$ [Fig. 2(f)], which is another evidence since the band structure, and consequently, the momentum-space Berry curvature, does not change much with temperature in this range. For temperature above T_N, the magnetic ground state changes, and thus AHE gradually deviates from the scaling relations, which is further discussed in the Supplemental Material [29].

If the field-dependent σ^{NA}_{xy} is the intrinsic Hall conductivity, its most likely origin is *a priori* the large Berry curvature from Weyl nodes. In order to clarify its physical origin in $EuCd_2As_2$, we performed high-resolution angle-resolved photoemission spectroscopy (ARPES) measurements. The measured band dispersion along the Γ-*K* direction at 7.9 K is shown in Fig. 3(b). Figure 3(a) is the corresponding Fermi surface integrated over a [E_F–50 meV, E_F + 50 meV] window. Several holelike bands cross the Fermi level, forming hole pockets. The weak spin canting at a temperature below T_N leads to the band splitting, which is well reproduced by our calculated band structure with a small canting angle [Figs. 3(b) and 3(c)]. According to our comprehensive band structure calculations (Fig. S8 [29]) and previous calculation results [22–27], the calculated Fermi level position, however, is above these holelike bands along the Γ-*K* direction. The Fermi level should not cross any bands, whatever the magnetic state is. Comparison between ARPES and first-principles calculation indicates that our sample has an unintentional *p* doping, which brings down the Fermi level 80–100 meV from the calculated one [Fig. 3(b)]. This might be due to the sensitive dependence of the Fermi energy on growth conditions. As a consequence, the Weyl node is about 100 meV above the real Fermi level, much larger than the energy of thermal fluctuations and band broadening at low temperatures. To this end, we conclude that Weyl physics should not determine the transport properties in our sample.

Alternatively, we show below that the giant nonlinear AHE is originated from the magnetic-field-induced band structure variation induced by spin canting. A series of spin configurations with various canting angles has been considered theoretically. Figure 3(d) shows the band structure and the

calculated intrinsic Hall conductivities σ_{xy}^{I} when the canting angle is 45°. The Fermi level of our sample lies between −80 and −100 meV (two red lines) estimated above, crossing a small gap at the Γ point. We find a prominent enhancement of σ_{xy}^{I} exactly in this range which should contribute significantly to the measured Hall conductivity. Figure 3(e) shows the evolution of band structures along K-Γ-A as the canting angle changes. Here, only bands around the Fermi energy are marked in order to clearly reveal the band evolution process and avoid distraction from irrelevant band hybridizations. For a collinear antiferromagnetic ground state with zero canting angle, all bands are degenerate and protected by the Kramers degeneracy and inversion symmetry, resulting in zero σ_{xy}^{I}. When spins are canted, time-reversal symmetry is broken, so that the degeneracy is lifted and each band splits into two branches. Band crossing between branches from different original bands occurs and contributes significantly to nonzero σ_{xy}^{I} (Fig. S9 [29]). In particular, the red and blue branches that split from the same valence band cross each other near the Γ point. Meanwhile, the yellow band gradually gets closer to the crossing point with increasing canting angles, touching the blue band at the canting angle of 45°. As a result, band hybridization and band inversion between these three branches occur, developing a small gap near the Fermi level that causes the largest σ_{xy}^{I}. However, with the further rise of the yellow band, band inversion occurs again and the band crossing is recovered at 63.43°. Eventually, at large fields, all spins are polarized along the c axis. σ_{xy}^{I} saturates to a fixed value that contributes to AHE σ_{xy}^{A} in our analysis. The band structure and the corresponding σ_{xy}^{I} at different canting angles are shown in Fig. S9 [29], from which we can confirm that σ_{xy}^{I} is indeed enhanced while the Fermi energy lies near the band crossing point or inside the band gap. Keeping the energy fixed near E_F (−80 to −100 meV), the variation of the calculated σ_{xy}^{I} as a function of canting angle is shown in Fig. 3(f). A peak at finite canting is obtained, consistent with the experimental observation in Fig. 2(e). The peak value varies between 70 and 100 S/cm, in the same range as the experimental value, and is sensitive to the Fermi energy. Actually, the peak feature is persistent in an even larger window of the Fermi energy from $E_F = -40$ meV to $E_F = -100$ meV (Fig. S10 [29]). The above calculations are based on the AFM ground states at $T < T_N$. Although the magnetic ground state changes above T_N, the spins also tilt with the external magnetic field and a similar argument is also suitable. We thus fully confirm that the THE-like feature in $EuCd_2As_2$ is indeed the intrinsic AHE, produced through a mechanism involving magnetic-field-induced changes in the band structure.

Finally, the momentum-space Berry curvature in $EuCd_2As_2$ is sensitive not only to the intensity but also to the direction of the external magnetic field. The results are summarized in Fig. 4 and the rotation geometry is depicted in the inset of Fig. 4(a). α is defined as the angle between the external magnetic field and the [001] direction. $\alpha = 0°$ and $\alpha = 90°$ correspond to the out-of-plane and the in-plane magnetic fields, respectively. The longitudinal resistivity $\rho_{xx}(B)$ increases monotonously with increasing α, showing an anisotropic behavior. However, surprisingly, the peak value of the Hall resistivity $\rho_{xy}(B)$ [Fig. 4(a)] reaches a

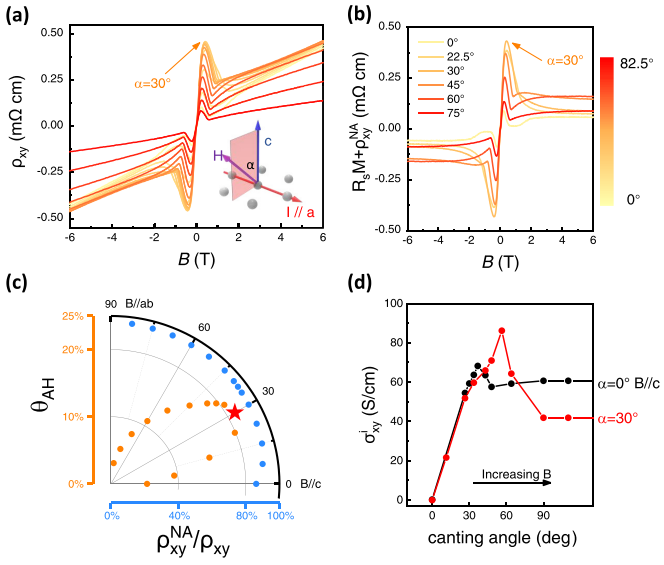

FIG. 4. Angle-dependent nonlinear AHE in $EuCd_2As_2$. (a) Magnetic-field dependence of the Hall resistance ρ_{xy} at different angles at $T = 2$ K. (b) Total anomalous Hall resistivity at different angles. The maximum nonlinear AHE appears at around $\alpha = 30°$. (c) Maximum anomalous Hall angle (yellow) and approximate nonlinear AHE ratio (blue) at different angles. The anomalous Hall angle can reach 21% at $\alpha = 30°$. (d) Calculated canting-dependent $|\sigma_{xy}^{I}|$ at different magnetic-field directions with $E_F = -94$ meV.

maximum at around $\alpha = 30°$, which is in contradiction with the conventional $\cos\alpha$ dependence of the anisotropic Hall resistivity. This provides another evidence of the important role that the spin canting plays in tuning the band structure. Since the nonlinear AHE is nearly one order of magnitude larger than the linear AHE at the peak position, here we simply plot $\rho_{xy}^{NA} + R_s M$ [Fig. 4(b)]. The anomalous Hall angle and the approximated nonlinear AHE ratio at different α are shown in Fig. 4(c). ρ_{xy}^{NA} and θ_{AH} can be greatly enhanced by tilting the magnetic field away from the [001] direction, reaching maximum values of 430 $\mu\Omega$ cm and 21% at $\alpha = 30°$, respectively, which is nearly 5 times larger than that at $\alpha = 0°$. Meanwhile, the nonlinear AHE always dominates the total Hall signals, with the approximate contribution ratio always larger than 80% from $\alpha = 0°$ to $\alpha = 90°$. Two main features from the angle-dependent transport measurements, i.e., the enhancement of the peak value and the change of the peak position, can both be well reproduced by additional calculations [Fig. 4(d)]. They originate from a similar band structure evolution process while the spins tilt from in-plane AFM structure to a forced FM structure along $\alpha = 30°$ instead of the [001] direction. But since this spin rotation process under a tilted external magnetic field is not well defined, the calculation results might show some variations from the real cases.

III. CONCLUSION

In conclusion, we have observed a giant nonlinear intrinsic AHE in $EuCd_2As_2$ which fully dominates the Hall response. We have shown that it originates from magnetic-field-induced

transitions in the band structure caused as a consequence of spin canting. We thus provide a general mechanism for nonmonotonous Hall response, which does not need strict magnetic or electron structures such as skyrmions or Weyl points. This effect has been completely overlooked in the past and may be suitable for some materials where the THE-like feature has not been well explained [19]. Our finding further raises the question of whether the THE-like feature can be originated from the combination of real-space spin chirality and spin-rotation-induced band structure evolution, which needs more research effort in the future.

IV. METHOD

A. Sample synthesis

Single crystals of $EuCd_2As_2$ were grown by the Sn flux method. High-purity elements of Eu, Cd, As, and Sn were put in an alumina crucible at a molar ratio of 1:2:2:10 and sealed in a quartz tube under a high vacuum. The tube was heated to 1173 K, remained at that temperature for 20 h, and then slowly cooled to 773 K at a rate of 2 K/h. After that, the samples were separated from the Sn liquid in a centrifuge.

B. Transport measurement

Transport measurements were performed in a Physical Property Measurement System (Quantum Design) with the standard lock-in technique. The electron contact of the sample is made into a standard six-point Hall bar. To correct the contact misalignment, the measured longitudinal and transverse voltages were field symmetrized and antisymmetrized, respectively.

C. ARPES measurement

The synchrotron ARPES measurements were performed at Beamline 03U of Shanghai Synchrotron Radiation Facility (SSRF). Data were collected by Scienta DA30 analyzer with a variable UV photon energy of 25–70 eV. The overall energy resolution is 15–18 meV, and the angular resolution was 0.2°. The sample was cleaved *in situ* and measured under an ultrahigh vacuum of 7×10^{-11} Torr.

D. Monte Carlo calculation

Spin interaction in the Monte Carlo simulations was modeled as

$$\begin{aligned} H = &-\sum_{\langle i,j\rangle} J\boldsymbol{m}_i \cdot \boldsymbol{m}_j - B\sum_{\mathrm{i}} m_i^z \\ &-\frac{16}{9}\sum_i K_1[(\boldsymbol{m}_{\mathrm{i}}\cdot\boldsymbol{u}^1)^2(\boldsymbol{m}_{\mathrm{i}}\cdot\boldsymbol{u}_2)^2 + (\boldsymbol{m}_{\mathrm{i}}\cdot\boldsymbol{u}_2)^2(\boldsymbol{m}_{\mathrm{i}}\cdot\boldsymbol{u}_3)^2 \\ &+(\boldsymbol{m}_{\mathrm{i}}\cdot\boldsymbol{u}_3)^2(\boldsymbol{m}_{\mathrm{i}}\cdot\boldsymbol{u}_1)^2] \\ &-16\sum_i K_2[(\boldsymbol{m}_{\mathrm{i}}\cdot\boldsymbol{u}^1)^2(\boldsymbol{m}_{\mathrm{i}}\cdot\boldsymbol{u}_2)^2(\boldsymbol{m}_{\mathrm{i}}\cdot\boldsymbol{u}_3)^2], \end{aligned}$$

where the first term is the nearest neighbor Heisenberg interaction, the second term is the Zeeman coupling, and the remaining two terms are sixth-order magnetocrystalline anisotropy, which is responsible for six preferred spin orientations in the plane. The parameters used in the simulations are $J_{xy} = 50k_B$, $J_z = -10k_B$, $K_1 = 2k_B$, $K_2 = 4k_B$, $B_z = 1.5k_B$, $u_1 = (-\frac{1}{2}, -\frac{\sqrt{3}}{2}, 0)$, $u_2 = (1, 0, 0)$, $u_3 = (-\frac{1}{2}, \frac{\sqrt{3}}{2}, 0)$. The system size is $256 \times 256 \times 2$. The periodical boundary condition was applied in both the x and y directions, while an open boundary condition was used for the z direction. All Monte Carlo simulations were carried out in our JUMAG software, which is a graphics processing unit (GPU)-accelerated package for spin dynamics and atomistic simulations [38]. The investigated systems were gradually cooled down from 500 to 0.1 K, and 50 000 Monte Carlo steps were performed for each temperature in order to sufficiently thermalize the system. At each sampled temperature, the topological charge distribution has been counted over 20 000 samples. Two neighboring samples were separated by 500 Monte Carlo steps.

E. Band structure calculations

The total energies and band structures were calculated from first-principles calculations within the framework of density functional theory using the projector augmented wave pseudopotential [39] as implemented in VASP [40,41]. The generalized gradient approximation of Perdew, Burke, and Ernzerhof [42] was used for the exchange-correlation energy and the Hubbard U method [43] with $U = 6.0$ eV and $J = 1.0$ eV was applied on the Eu($4f$) orbitals. An energy cutoff 600 eV for the plane-wave expansion was used. Noncollinear magnetism calculations with spin-orbit coupling included were employed. A $1 \times 1 \times 2$ supercell with two Eu atoms was used and a Γ-centered $15 \times 15 \times 4$ k mesh was sampled. After we obtained the eigenstates and eigenvalues, a unitary transformation of Bloch waves was performed to construct the tight-binding Hamiltonian in a Wannier function (WF) basis by using the maximally localized Wannier functions method [44] implemented in the WANNIER90 package [45]. A WF-based Hamiltonian has exactly the same eigenvalues as those obtained by first-principles calculations from −0.5–0.5 eV to the Femi level. The intrinsic anomalous Hall conductivity was calculated using the WF-based Hamiltonian based on Berry curvature [46].

Note added. During the review process, we note that a recent study of $SrRuO_3$ [47] also reveals its anomalous Hall effect to be sensitive to the spin tilting due to the evolution of Berry curvature.

ACKNOWLEDGMENTS

F.X. was supported by the National Natural Science Foundation of China (Grants No. 52150103, No. 11934005, and No. 11874116), National Key Research and Development Program of China (Grants No. 2017YFA0303302 and No. 2018YFA0305601), the Science and Technology Commission of Shanghai (Grant No. 19511120500), the Shanghai Municipal Science and Technology Major Project (Grant No. 2019SHZDZX01), the Program of Shanghai Academic/Technology Research Leader (Grant No. 20XD1400200), and Shanghai Pilot Program for Basic Research – FuDan University 21TQ1400100 (21TQ006). Work at UNH was supported by the U.S. Department of Energy,

Office of Science, Basic Energy Sciences (Grant No. DE-SC0020221). R.P. was supported by the National Natural Science Foundation of China (Grant No. 11922403). Y.S. was supported by the Chinese National Key Research and Development Program (Grant No. 2017YFA0302901), the National Natural Science Foundation of China (Grants No. U2032204 and No. 12004416), the Strategic Priority Research Program (B) of the Chinese Academy of Sciences (Grant No. XDB33000000). L.K. was supported by the National Natural Science Foundation of China (Grant No. 11974021). We thank Cheng Zhang, Xingtai Chen, Wenqing Liu, and Zhongkai Liu for their insightful discussions. Part of the sample fabrication was performed at Fudan Nano-fabrication Laboratory.

[1] N. Nagaosa, J. Sinova, S. Onoda, A. H. MacDonald, and N. P. Ong, Anomalous Hall effect, Rev. Mod. Phys. **82**, 1539 (2010).

[2] N. Nagaosa and Y. Tokura, Topological properties and dynamics of magnetic skyrmions, Nat. Nanotechnol. **8**, 899 (2013).

[3] Y. Taguchi, Y. Oohara, H. Yoshizawa, N. Nagaosa, and Y. Tokura, Spin chirality, Berry phase, and anomalous Hall effect in a frustrated ferromagnet, Science **291**, 2573 (2001).

[4] T. Kurumaji, T. Nakajima, M. Hirschberger, A. Kikkawa, Y. Yamasaki, H. Sagayama, H. Nakao, Y. Taguchi, T. Arima, and Y. Tokura, Skyrmion lattice with a giant topological Hall effect in a frustrated triangular-lattice magnet, Science **365**, 914 (2019).

[5] L. Vistoli, W. Wang, A. Sander, Q. Zhu, B. Casals, R. Cichelero, A. Barthélémy, S. Fusil, G. Herranz, S. Valencia, R. Abrudan, E. Weschke, K. Nakazawa, H. Kohno, J. Santamaria, W. Wu, V. Garcia, and M. Bibes, Giant topological Hall effect in correlated oxide thin films, Nat. Phys. **15**, 67 (2019).

[6] W. Wang, M. W. Daniels, Z. Liao, Y. Zhao, J. Wang, G. Koster, G. Rijnders, C.-Z. Chang, D. Xiao, and W. Wu, Spin chirality fluctuation in two-dimensional ferromagnets with perpendicular magnetic anisotropy, Nat. Mater. **18**, 1054 (2019).

[7] C. Sürgers, G. Fischer, P. Winkel, and H. v Löhneysen, Large topological Hall effect in the non-collinear phase of an antiferromagnet, Nat. Commun. **5**, 3400 (2014).

[8] A. Neubauer, C. Pfleiderer, B. Binz, A. Rosch, R. Ritz, P. G. Niklowitz, and P. Böni, Topological Hall Effect in the *A* Phase of MnSi, Phys. Rev. Lett. **102**, 186602 (2009).

[9] H. Kawamura, Anomalous Hall Effect as a Probe of the Chiral Order in Spin Glasses, Phys. Rev. Lett. **90**, 047202 (2003).

[10] Y. Machida, S. Nakatsuji, S. Onoda, T. Tayama, and T. Sakakibara, Time-reversal symmetry breaking and spontaneous Hall effect without magnetic dipole order, Nature (London) **463**, 210 (2010).

[11] H. Chen, Q. Niu, and A. H. MacDonald, Anomalous Hall Effect Arising from Noncollinear Antiferromagnetism, Phys. Rev. Lett. **112**, 017205 (2014).

[12] C. Shekhar, N. Kumar, V. Grinenko, S. Singh, R. Sarkar, H. Luetkens, S.-C. Wu, Y. Zhang, A. C. Komarek, E. Kampert, Y. Skourski, J. Wosnitza, W. Schnelle, A. McCollam, U. Zeitler, J. Kübler, B. Yan, H.-H. Klauss, S. S. P. Parkin, and C. Felser, Anomalous Hall effect in Weyl semimetal half Heusler compounds *R*PtBi (R = Gd and Nd), Proc. Natl. Acad. Sci. USA **115**, 9140 (2018).

[13] Y. Zhu, B. Singh, Y. Wang, C.-Y. Huang, W.-C. Chiu, B. Wang, D. Graf, Y. Zhang, H. Lin, J. Sun, A. Bansil, and Z. Mao, Exceptionally large anomalous Hall effect due to anticrossing of spin-split bands in the antiferromagnetic half-Heusler compound TbPtBi, Phys. Rev. B **101**, 161105(R) (2020).

[14] H. Zhang, Y. L. Zhu, Y. Qiu, W. Tian, H. B. Cao, Z. Q. Mao, and X. Ke, Field-induced magnetic phase transitions and the resultant giant anomalous Hall effect in the antiferromagnetic half-Heusler compound DyPtBi, Phys. Rev. B **102**, 094424 (2020).

[15] T. Suzuki, R. Chisnell, A. Devarakonda, Y.-T. Liu, W. Feng, D. Xiao, J. W. Lynn, and J. G. Checkelsky, Large anomalous Hall effect in a half-Heusler antiferromagnet, Nat. Phys. **12**, 1119 (2016).

[16] R. Singha, S. Roy, A. Pariari, B. Satpati, and P. Mandal, Magnetotransport properties and giant anomalous Hall angle in the half-Heusler compound tbptbi, Phys. Rev. B **99**, 035110 (2019).

[17] Z. Fang, N. Nagaosa, K. S. Takahashi, A. Asamitsu, R. Mathieu, T. Ogasawara, H. Yamada, M. Kawasaki, Y. Tokura, and K. Terakura, The anomalous Hall effect and magnetic monopoles in momentum space, Science **302**, 92 (2003).

[18] Y. Xu, L. Das, J. Z. Ma, C. J. Yi, S. M. Nie, Y. G. Shi, A. Tiwari, S. S. Tsirkin, T. Neupert, M. Medarde, M. Shi, J. Chang, and T. Shang, Unconventional Transverse Transport above and below the Magnetic Transition Temperature in Weyl Semimetal $EuCd_2As_2$, Phys. Rev. Lett. **126**, 076602 (2021).

[19] Y. Chen, Y.-W. Chuang, S. H. Lee, Y. Zhu, K. Honz, Y. Guan, Y. Wang, K. Wang, Z. Mao, J. Zhu, C. Heikes, P. Quarterman, P. Zajdel, J. A. Borchers, and W. Ratcliff, Ferromagnetism in van der Waals compound $MnSb_{1.8}Bi_{0.2}Te_4$, Phys. Rev. Mater. **4**, 064411 (2020).

[20] P. Vir, J. Gayles, A. S. Sukhanov, N. Kumar, F. Damay, Y. Sun, J. Kübler, C. Shekhar, and C. Felser, Anisotropic topological Hall effect with real and momentum space Berry curvature in the antiskrymion-hosting Heusler compound $Mn_{1.4}PtSn$, Phys. Rev. B **99**, 140406(R) (2019).

[21] M. C. Rahn, J.-R. Soh, S. Francoual, L. S. I. Veiga, J. Strempfer, J. Mardegan, D. Y. Yan, Y. F. Guo, Y. G. Shi, and A. T. Boothroyd, Coupling of magnetic order and charge transport in the candidate Dirac semimetal $EuCd_2As_2$, Phys. Rev. B **97**, 214422 (2018).

[22] J.-R. Soh, F. de Juan, M. G. Vergniory, N. B. M. Schröter, M. C. Rahn, D. Y. Yan, J. Jiang, M. Bristow, P. Reiss, J. N. Blandy, Y. F. Guo, Y. G. Shi, T. K. Kim, A. McCollam, S. H. Simon, Y. Chen, A. I. Coldea, and A. T. Boothroyd, Ideal Weyl semimetal induced by magnetic exchange, Phys. Rev. B **100**, 201102(R) (2019).

[23] J.-Z. Ma, S. M. Nie, C. J. Yi, J. Jandke, T. Shang, M. Y. Yao, M. Naamneh, L. Q. Yan, Y. Sun, A. Chikina, V. N. Strocov, M. Medarde, M. Song, Y.-M. Xiong, G. Xu, W. Wulfhekel, J. Mesot, M. Reticcioli, C. Franchini, C. Mudry *et al.*, Spin fluctuation induced Weyl semimetal state in the paramagnetic phase of $EuCd_2As_2$, Sci. Adv. **5**, eaaw4718 (2019).

[24] L.-L. Wang, N. H. Jo, B. Kuthanazhi, Y. Wu, R. J. McQueeney, A. Kaminski, and P. C. Canfield, Single pair of Weyl fermions in the half-metallic semimetal $EuCd_2As_2$, Phys. Rev. B **99**, 245147 (2019).

[25] G. Hua, S. Nie, Z. Song, R. Yu, G. Xu, and K. Yao, Dirac semimetal in type-IV magnetic space groups, Phys. Rev. B **98**, 201116(R) (2018).

[26] K. M. Taddei, L. Y. Lin, L. D. Sanjeewa, J. Xing, C. dela Cruz, and D. Parker, Spin-canting driven Weyl physics in $EuCd_2As_2$, arXiv:2012.01555 [cond-mat.str-el].

[27] J. Ma, H. Wang, S. Nie, C. Yi, Y. Xu, H. Li, J. Jandke, W. Wulfhekel, Y. Huang, D. West, P. Richard, A. Chikina, V. N. Strocov, J. Mesot, H. Weng, S. Zhang, Y. Shi, T. Qian, M. Shi, and H. Ding, Emergence of nontrivial low-energy Dirac fermions in antiferromagnetic $EuCd_2As_2$, Adv. Mater. **32**, 1907565 (2020).

[28] J.-R. Soh, E. Schierle, D. Y. Yan, H. Su, D. Prabhakaran, E. Weschke, Y. F. Guo, Y. G. Shi, and A. T. Boothroyd, Resonant x-ray scattering study of diffuse magnetic scattering from the topological semimetals $EuCd_2As$ and $EuCd_2Sb_2$, Phys. Rev. B **102**, 014408 (2020).

[29] See Supplemental Material at http://link.aps.org/supplemental/10.1103/PhysRevResearch.4.023100 for more characterizations of the sample, magnetization measurement results, decomposition procedure of the Hall resistivity and conductivity, transport measurement results of additional samples, and more details on the band-structure and anomalous Hall conductivity calculations.

[30] Y. Ohuchi, Y. Kozuka, M. Uchida, K. Ueno, A. Tsukazaki, and M. Kawasaki, Topological Hall effect in thin films of the Heisenberg ferromagnet EuO, Phys. Rev. B **91**, 245115 (2015).

[31] P. K. Rout, P. V. Prakash Madduri, S. K. Manna, and A. K. Nayak, Field-induced topological Hall effect in the noncoplanar triangular antiferromagnetic geometry of Mn_3Sn, Phys. Rev. B **99**, 094430 (2019).

[32] H. Li, B. Ding, J. Chen, Z. Li, E. Liu, X. Xi, G. Wu, and W. wang, Large anisotropic topological Hall effect in a hexagonal non-collinear magnet Fe_5Sn_3, Appl. Phys. Lett. **116**, 182405 (2020).

[33] N. Kanazawa, Y. Onose, T. Arima, D. Okuyama, K. Ohoyama, S. Wakimoto, K. Kakurai, S. Ishiwata, and Y. Tokura, Large Topological Hall Effect in a Short-Period Helimagnet MnGe, Phys. Rev. Lett. **106**, 156603 (2011).

[34] C. Franz, F. Freimuth, A. Bauer, R. Ritz, C. Schnarr, C. Duvinage, T. Adams, S. Blügel, A. Rosch, Y. Mokrousov, and C. Pfleiderer, Real-Space and Reciprocal-Space Berry Phases in the Hall Effect of $Mn_{1-x}Fe_xSi$, Phys. Rev. Lett. **112**, 186601 (2014).

[35] B. M. Ludbrook, G. Dubuis, A.-H. Puichaud, B. J. Ruck, and S. Granville, Nucleation and annihilation of skyrmions in Mn_2CoAl observed through the topological Hall effect, Sci. Rep. **7**, 13620 (2017).

[36] W. Zhang, B. Balasubramanian, A. Ullah, R. Pahari, X. Li, L. Yue, S. R. Valloppilly, A. Sokolov, R. Skomski, and D. J. Sellmyer, Comparative study of topological Hall effect and skyrmions in NiMnIn and NiMnGa, Appl. Phys. Lett. **115**, 172404 (2019).

[37] Y. Wang, C. Xian, J. Wang, B. Liu, L. Ling, L. Zhang, L. Cao, Z. Qu, and Y. Xiong, Anisotropic anomalous Hall effect in triangular itinerant ferromagnet Fe_3GeTe_2, Phys. Rev. B **96**, 134428 (2017).

[38] JUMAG—A JULIA package for classical spin dynamics and micromagnetic simulations with GPU support (2019), https://github.com/ww1g11/JuMag.jl.

[39] G. Kresse and D. Joubert, From ultrasoft pseudopotentials to the projector augmented-wave method, Phys. Rev. B **59**, 1758 (1999).

[40] G. Kresse and J. Furthmüller, Efficient iterative schemes for *ab initio* total-energy calculations using a plane-wave basis set, Phys. Rev. B **54**, 11169 (1996).

[41] G. Kresse and J. Furthmüller, Efficiency of *ab-initio* total energy calculations for metals and semiconductors using a plane-wave basis set, Comput. Mater. Sci. **6**, 15 (1996).

[42] J. P. Perdew, K. Burke, and M. Ernzerhof, Generalized Gradient Approximation Made Simple, Phys. Rev. Lett. **77**, 3865 (1996).

[43] A. I. Liechtenstein, V. I. Anisimov, and J. Zaanen, Density-functional theory and strong interactions: Orbital ordering in Mott-Hubbard insulators, Phys. Rev. B **52**, R5467 (1995).

[44] N. Marzari, A. A. Mostofi, J. R. Yates, I. Souza, and D. Vanderbilt, Maximally localized Wannier functions: Theory and applications, Rev. Mod. Phys. **84**, 1419 (2012).

[45] A. A. Mostofi, J. R. Yates, G. Pizzi, Y.-S. Lee, I. Souza, D. Vanderbilt, and N. Marzari, An updated version of WANNIER90: A tool for obtaining maximally-localised Wannier functions, Comput. Phys. Commun. **185**, 2309 (2014).

[46] X. Wang, J. R. Yates, I. Souza, and D. Vanderbilt, *Ab initio* calculation of the anomalous Hall conductivity by Wannier interpolation, Phys. Rev. B **74**, 195118 (2006).

[47] D. Tian, Z. Liu, S. Shen, Z. Li, Y. Zhou, H. Liu, H. Chen, and P. Yu, Manipulating Berry curvature of $SrRuO_3$ thin films via epitaxial strain, Proc. Natl. Acad. Sci. USA **118**, e2101946118 (2021).